

Article

Effect of Saturated Steam Carried Downward on the Flow Properties in the Downcomer of Steam Generator

Yan Liu ^{1,2}, Hui-lie Shi ², Chun Gui ², Xian-yuan Wang ^{1,2,*} and Rui-feng Tian ²

¹ Fundamental Science on Nuclear Safety and Simulation Technology Laboratory, Harbin Engineering University, Harbin 150001, China

² Research Institute of Nuclear Power Operation, Wuhan 430223, China

* Correspondence: wangxy08@cnpn.com.cn; Tel.: +86-1397-113-0686

Received: 2 September 2019; Accepted: 20 September 2019; Published: 24 September 2019



Abstract: The saturated water separated by the steam separator in a natural circulation steam generator may carry a small amount of saturated steam into the downcomer. The steam contacts subcooled water and condenses directly in the downcomer causing the variations in the pressure and steam quality and likely affecting the stability of the water cycle in the secondary loop. It is not conducive to core heat extraction and thus affects nuclear safety. The mathematical model of the downcomer was established in this study based on the internal structures of a natural circulation steam generator. The volume-of-fluid (VOF) and large-eddy-simulation (LES) models were used for analysis on FLUENT software (ANSYS, Pittsburgh, PA, USA) platform. The influence of direct contact condensation of top-down flowing steam on the flow properties in the downcomer of the steam generator under high pressure was studied. The trend of the temperature, pressure, and the void fraction were obtained by combining these models with the condensation model. Further, a one-dimensional calculation program based on the differential drop was also developed to assess the flow field in the downcomer. The calculation results are in good agreement with the experimental results which indicated that, when affected by the saturated steam carried downward, the flow temperature close to the exit of the downcomer rises slightly due to the absorption of the heat released by the steam condensation. Furthermore, the density corrected by the pressure-drop is more reliable than that corrected by the temperature. After the velocity in the downcomer has increased to a certain value, the sensitivity of steam quality to the subcooling degree in the downcomer begins to decline. The results in this paper can be used to perform stability analyses and to design steam generators. The results of research are helpful to the stability analysis and the design of a steam generator, and to improve the accuracy of the measurement of the steam generator operating parameters, thus enhancing the safety of Pressurize Water Reactor operating system.

Keywords: direct contact and condensation of steam; natural circulation steam generator; downcomer; condensation model

1. Introduction

A natural circulation steam generator is a critical part of the nuclear power plant equipment [1]. It is mainly used to absorb the heat of reactor coolant as well as to generate the saturated steam that drives a steam turbine. The basic circulation loop of a natural circulation steam generator is composed of an ascending channel, a steam separator, and a downcomer [2]. As shown in Figure 1, the feed water flows from the feed pipe into the steam generator and from the top to bottom along the downcomer. The feed water flows over the support plate into the ascending channel and absorbs heat in the ascending channel to generate saturated steam. This saturated steam is then filtered out by the

steam separator, while the water filtered by the steam separator, known as recycled water, carries part of the steam, mixes it with the feed water, and flows along the downcomer. Since the density of the water in the downcomer is greater than the steam mixture in the ascending channel, the water flows down the downcomer, whereas the mixture flows up the ascending channel.

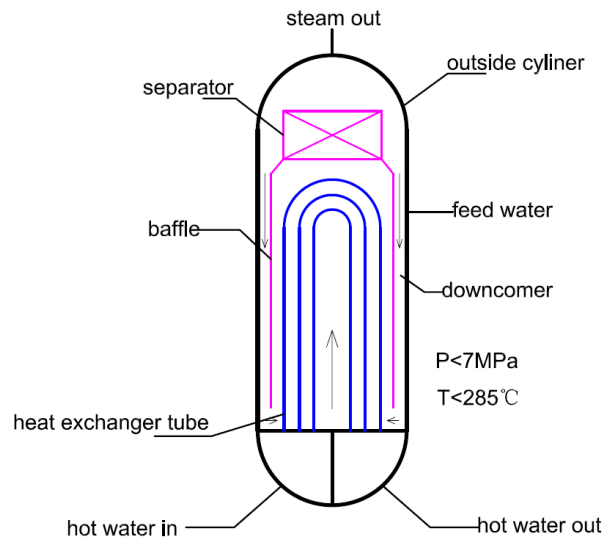


Figure 1. Schematic diagram of the steam generator simulator.

The following relationship can be assumed under the condition that the water circulation is stable [2]:

$$P + \rho_m g H - \Delta P_{dc} = P + \rho_x g H_x + \rho_{xs} g H_{xs} - \Delta P_r - \Delta P_{sp} \quad (1)$$

where P is the steam pressure, ρ_m is the density of the downcomer, H is the height of the downcomer, ρ_x is the density of the pre-heating section in the ascending channel, H_x is the height of the pre-heating section, ρ_{xs} is the density of the vapor section in the ascending channel, H_{xs} is the height of the vapor section, ΔP_r is the ascending channel resistance, and ΔP_{sp} is the steam separator resistance.

The left side of Equation (1) represents the driving force for the circulation of the steam generator's secondary loop, while the right side is its resistance. The saturated steam directly contacts the downcomer walls and condenses. This changes the density and resistance in the downcomer and might lead to the decrease of the density in the downcomer and the decrease of the driving force, thus affecting the stability of the water cycle in the secondary loop. Therefore, the study of this topic has certain research significance.

Woods et al. conducted six groups of different experiments based on the advanced plant experimental test facility (APEX) for AP600 in the Oregon State University [3]. These experiments were aimed to evaluate the steam condensation rate of an established scaled model [3,4] of steam generators under different pressures and inlet flow rates of primary and secondary loops. Brucker and Sparrow researched the direct contact and condensation of steam bubbles under high-pressure conditions [5]. The process was simulated from below through the experiments at 1–6 MPa. Their study illustrated that the time for steam bubbles to collapse increases with increasing pressure but decreases when the subcooling degree rises.

Numerical simulations have been carried out as well. Yang et al. established a three-dimensional physical model of a steam generator unit tube based on similarity theory using the steam generator of Daya Bay Nuclear Power Plant as a prototype [6]. The numerical simulations of the two-phase flow and boiling heat transfer properties at the secondary loop of the steam generator were performed via the CFX software (ANSYS, Pittsburgh, PA, USA) [7,8] using a particle model and a phase-transformation model [9]. However, the trend of the void fraction on the cross-section of a steam generator ascending channel was also investigated. Indeed, Jiang et al. established a computational model of a

three-dimensional flow at the secondary loop of the steam generator via FLUENT [10] software using a porous-medium model under the condition that it is single-phase flow at the secondary loop of the steam generator [11]. The three-dimensional flow field at the secondary loop of a steam generator during the steady-state operation of the nuclear power plant was computed, and the distribution of pressure and velocity for the entire flow field was obtained. Li et al. [12] performed a numerical simulation on the fluid flow in the feed-water pipe and downcomer via the CFX software using the re-normalization group (RNG) k - ϵ turbulence model [13]. Furthermore, the mixing of feed and recirculation water in the steam generator downcomer as well as the distribution of the flow rate and temperature were mainly investigated under a single-phase condition. Zhou et al. [14] investigated the shape variation of the steam column under different steam pressures using the Euler multiphase flow model [15], and the realizable k - ϵ turbulence [13] and thermal equilibrium change [13] models. Gulawani et al. carried out Computational Fluid Dynamics simulations of the direct contact and condensation of steam using a double-resistance model [16]. In their model, there was no resistance on the vapor-phase side, and the Ranz-Marshall model [17] was adopted in the liquid phase. The computational results were in good agreement with the experimental data. Li et al. conducted numerical simulations and mechanism analyses of the steam direct contact condensation in the t-shaped circular tubes by using the gas-liquid two-phase flow and large eddy simulation turbulence model [18] combined with the double-resistance model on the FLUENT platform. None of the above studies investigated the influence of the steam direct-contact condensation on the internal flow field of the steam generator under the top-down flow state in the downcomer of the steam generator.

This work aims to investigate the condensation state of saturated steam carried to the narrow downcomer of the steam generator in the direction of the top to bottom and its influence on the flow characteristics. The mathematical model of the downcomer was established based on the internal structures of natural circulation steam generator, and the volume-of-fluid (VOF) and large-eddy-simulation (LES) models combined with the condensation model were used for the analysis. A small steam generator simulator and an experiment loop were designed in accordance with a typical power plant system. To this end, the experimental and computational analyses were carried out.

2. Computational Analysis

According to the internal structure of the steam generator, the equation of mass, momentum, and energy conservation was established for the direct contact condensation process of steam and subcooled water in the downcomer of the steam generator. The phase change models of condensation and mass transfer at the vapor-liquid condensation interface were therefore built. An appropriate condensation heat and mass transfer model was also built and a user define function (UDF) was written and embeded in the Computational Fluid Dynamics software. The changes in the velocity field, temperature field, and pressure field during direct contact condensation were obtained.

2.1. Physical Model

As shown in Figure 2, the actual physical model was reconstructed in equal proportions. The inlet section of the vapor mixture, the width of the downcomer, and the size of the subcooled water inlets are consistent with the real object. The inlet diameters of the three subcooled water inlets are 3.74 mm; the inlet inner diameter of the soda mixture is 966 mm, while the inlet outer diameter is 1266 mm; finally, the width of the downcomer is 23 mm.

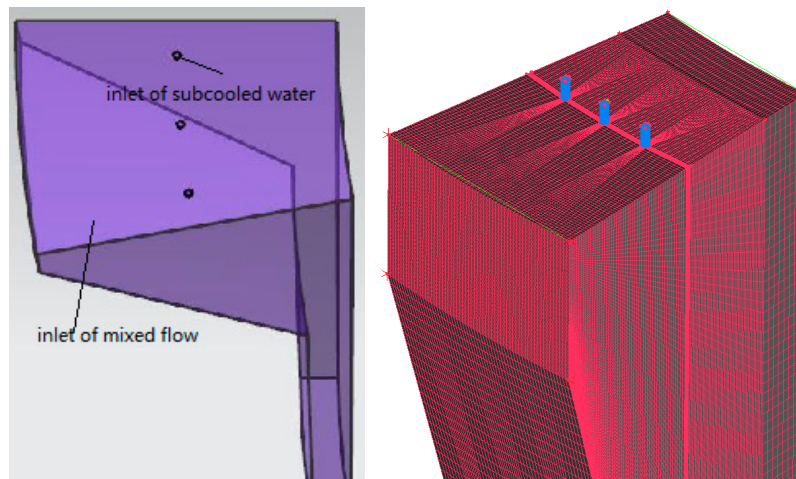


Figure 2. Schematic diagram of the physical model.

The inlet velocity of subcooled water was set as 11 m/s, while the flow mixed with saturated water and vapor was 0.12 m/s. The temperature of the mixture was the saturation temperature under the operating pressure, and the vapor rate of the mixture was 0.5%.

The commercial software ANSYS/ICEM [19] was used to draw three kinds of hexahedral structured grids with different quantities and the mesh quantities were 723,030, 1,584,664, and 2,441,390, respectively. The grids of the subcooled water inlet were encrypted, the number of boundary layer grids was 10, and the y^+ values corresponding to three different numbers of grids in the numerical calculation process were 70–90, 15–20, and 10, respectively. Based on the above three different amounts of grids, the temperature at the center of the section at the top of the downcomer was monitored over time. As shown in Figure 3, when the mesh quantity was 1,584,664 and 2,141,390, the temperature changed with time with the same trend with most of the errors being within 1%. In order to save time and cost, the second grid number was adopted for further simulations.

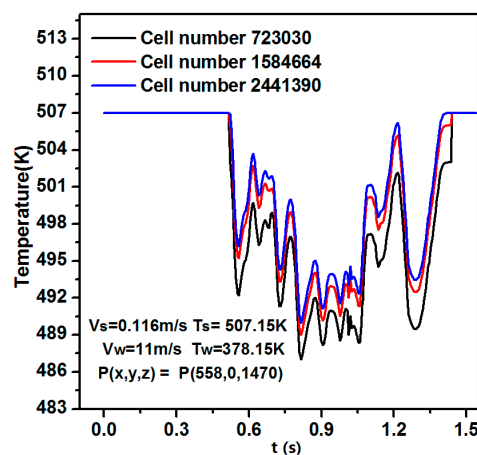


Figure 3. Temperature curve of the top section at different times.

Where V_s is the inlet velocity of the vapor mixture; V_m is the inlet velocity of the subcooled water; T_s is temperature of the vapor mixture; T_w is temperature of the subcooled water; and P is the pressure at the coordinate point.

2.2. Mathematical Model

A VOF multiphase model tracked the location of the vapor-liquid interface in real time, while a LES model [18] was employed to capture the pulsation characteristics of turbulence.

(1) Control equation

The VOF multiphase flow model control equation includes a continuity equation, a momentum equation, and an energy equation, as follows.

The continuity equation is [18]:

$$\frac{1}{\rho} \left[\frac{\partial}{\partial t} (\alpha_q \rho_q) + \nabla \cdot (\alpha_q \rho_q \mathbf{u}_q) \right] = S_{\alpha_q} + \sum_{p=1}^n (\dot{m}_{pq} - \dot{m}_{qp}) \quad (2)$$

$$\text{With } \sum_{q=1}^n \alpha_q = 1 \quad (3)$$

where \mathbf{u}_q is the velocity of phase q , m/s; α_q is the volume fraction of phase q ; \dot{m}_{pq} is the mass transfer from phase p to phase q , kg/s; \dot{m}_{qp} is the mass transfer from phase q to phase p , kg/s; and S_{α_q} is the quality source term.

The momentum equation is [18]:

$$\left[\frac{\partial}{\partial t} (\rho \mathbf{u}) + \nabla \cdot (\rho \mathbf{u} \mathbf{u}) \right] = -\nabla P + \nabla \cdot [\mu (\nabla \mathbf{u} + \nabla \mathbf{u}^T)] + \rho \mathbf{g} + \mathbf{F} \quad (4)$$

where ρ is the density, kg/m³; μ is the dynamic viscosity, kg/(m·s); \mathbf{u} is the velocity, m/s; \mathbf{F} is the volume force. Only the surface tension of two phases was considered in this numerical simulation.

The continuous surface force (CSF) model was adopted to determine the tension of the liquid phase:

$$\mathbf{F} = \mathbf{F}_{\text{CSF}} = \sigma \kappa \nabla \alpha \quad (5)$$

where κ is the curvature and σ is the surface tension coefficient.

The density and dynamic viscosity [18] used in Equation (4) are defined in Equations (6) and (7):

$$\rho = \alpha_2 \rho_2 + (1 - \alpha_2) \rho_1 \quad (6)$$

$$\mu = \alpha_2 \mu_2 + (1 - \alpha_2) \mu_1 \quad (7)$$

The energy equation can be written as [18]:

$$\left[\frac{\partial}{\partial t} (\rho E) + \nabla \cdot (\mathbf{u} (\rho E + P)) \right] = \nabla \cdot [(k_{\text{eff}} \nabla T)] + S_h \quad (8)$$

where E is the energy, p is the pressure, Pa; T is the temperature, K; k_{eff} is the effective thermal conductivity of the fluid, w/(m·K); and S_h is the energy source term.

(2) LES turbulence model

In the LES model, the n-s equation of incompressible fluid is filtered and its corresponding equation is obtained as follows [18].

$$\frac{\partial \rho}{\partial t} + \frac{\partial \rho \bar{u}_i}{\partial x_i} = 0 \quad (9)$$

$$\frac{\partial \rho \bar{u}_i}{\partial t} + \frac{\partial \rho \bar{u}_i \bar{u}_j}{\partial x_j} = -\frac{\partial \bar{P}}{\partial x_i} - \rho_0 \beta (T - T_0) g + \frac{\partial}{\partial x_j} \left[(\mu + \mu_t) \left(\frac{\partial \bar{u}_i}{\partial x_j} + \frac{\partial \bar{u}_j}{\partial x_i} \right) \right] \quad (10)$$

where μ is the dynamical viscosity, kg/(m·s); μ_t is the turbulent viscosity; and β is the coefficient of thermal expansion.

The Smagorinsky–Lilly [18] model was used for small scale vortices:

$$\mu_t = \rho L_s^2 |\bar{S}|^2 \quad (11)$$

where $|\bar{S}| = \sqrt{2\bar{S}_{ij}\bar{S}_{ji}}$. L_s is the sublattice-scale mixing length described as [18]:

$$L_s = \min(\kappa d, C_s V^{1/3}) \quad (12)$$

where κ is the Von Karman constant, set as 0.42; d is the distance between the cell and the nearest wall; V is the volume of the cell; and C_s is the Smagorinsky constant, set as 0.1.

(3) Condensation model

The condensation process in the downcomer was determined by using the condensation double-resistance model, which is based on the heat balance principle and can be used to calculate the condensation phenomenon caused by heat transfer between the two phases of pure material flow. The condensation double-resistance model assumes that one phase (vapor phase) is dispersed as a small spherical bubble with a variable diameter at the intersection interface. The heat and mass transfer occur on the bubble surface, while thermal resistance exists simultaneously at the intersection interface. The energy transfer of steam direct contact condensation depends on the phase-change interfacial area, the interfacial heat transfer coefficient, and the interfacial mass transfer rate.

In the liquid phase, the vapor-liquid interface area is [18]:

$$A_{ifg} = \frac{6\alpha_{ig}}{d_{ig}} \quad (13)$$

where α_{ig} is the steam volume fraction and d_{ig} is the average bubble diameter, which is given by Anglart and Nylundl [20]:

$$d_{ig} = \begin{cases} 1.5 \times 10^{-4} & \theta_i > 13.5 \\ \frac{d_1(\theta - \theta_0) + d_0(\theta_1 - \theta)}{\theta_1 - \theta_0} & 0 < \theta_i < 13.5 \\ 1.5 \times 10^{-3} & \theta_i \leq 0 \end{cases} \quad (14)$$

The mean bubble diameter is used to calculate the liquid Reynolds number and Nusselt number in the condensing double-resistance model.

The heat transfer coefficient of the liquid phase can be determined as [18]:

$$h_{if} = \frac{k_{if} Nu_{fi}}{d_{ig}} \quad (15)$$

Nusselt number of the liquid phase is determined according to the correlation given by Hughmark [21]:

$$Nu_{fi} = \begin{cases} 2.0 + 0.6Re^{0.5}Pr^{0.33} & 0 \leq Re < 766.06 \\ 2.0 + 0.27Re^{0.62}Pr^{0.33} & Re \geq 766.06 \end{cases} \quad (16)$$

The heat transfer quantity on the liquid phase side of per unit volume [15] can be calculated as:

$$H_{if} = h_{if} A_{ifg} \quad (17)$$

The changes in fluid properties can cause an abrupt increase in the condensation rate. Koncar and Mavlo [22] proposed the so-called umbrella restriction, through the constraint of which the sudden change in the condensation rate can be limited in some special cases, approaching that of actual situations:

$$H_{if} = \min\{H_{if}, 1753, 9\max[4.724, 472.4\alpha_{ig}(1 - \alpha_{ig})]\} \times \max[0, \min(1, \frac{\alpha_{ig} - 1.0 \times 10^{-10}}{0.1 - 1.0 \times 10^{-10}})] \quad (18)$$

The zero-resistance [18,20] model is applied from the interface at the vapor phase. The temperature on the vapor phase side of the interface approximates the saturation temperature at the operating pressure.

The heat flux of convective heat transfer from the phase-change interface to the liquid phase side is [18]:

$$q_{if} = h_{if}(t_{is} - t_{if}) \quad (19)$$

The total heat flux from the phase change interface to the liquid-phase side is [18]:

$$Q_{il} = q_{if} + m_{isl}H_{il} \quad (20)$$

where m_{isl} is the condensation rate, H_{il} is the saturated water enthalpy, whereas the total heat flux from the phase-change interface to the vapor phase side corresponds to [18]:

$$Q_{is} = m_{isl}H_{is} \quad (21)$$

H_{is} is the saturated steam enthalpy. Therefore, based on the total heat flux equilibrium at the phase change interface, it can be assumed that:

$$Q_{il} = Q_{is} \quad (22)$$

The steam condensation rate can be obtained from the above equations:

$$m_{isl} = \frac{q_{if}}{H_{is} - H_{il}} \quad (23)$$

2.3. Boundary Conditions

In the calculation of the boundary conditions, the void fraction of the inlet distributed evenly was set as 0.5%, while the inlet velocity was determined according to the flow and flow area. The effect of the wall thickness was neglected in the numerical model, and the adiabatic boundary condition of the solid wall was adopted [23].

The double-precision implicit unsteady solver, which was developed based on pressure, was selected for the numerical calculations. The SIMPLE [13] algorithm was adopted for the coupling of pressure and velocity, while the PRESTO [13] discrete format was adopted for the pressure term. The momentum equation, energy equation, and volume fraction were discretized by a bounded central difference, second-order upwind, and geometric reconstruction, respectively. The VOF two-phase flow model used an explicit discrete format. Since surface tension was involved in the calculation, the implicit body force had been chosen in the body force formulation to improve the convergence of solutions. The Smagorinsky-Lilly [18] subgrid model was selected for the LES turbulence model. The residual convergence standard of the energy equation was set as 1×10^{-6} , while the residual convergence standard of other variables was set as 1×10^{-3} .

Before the calculation begins, the saturated water and subcooled water were filled in the calculation domain and the subcooled water inlet by the Patch method [13].

The thermo-physical properties of the subcooled water and saturated steam, such as the saturation temperature at local pressure and the enthalpy of steam and water at the corresponding saturation temperature, were derived from National Institute Standard Technology (NIST).

Through nonlinear fitting of relevant data derived from NIST, the relationships between the abovementioned physical properties of steam and water were obtained. These relationships were entered into the parallel UDF program of the double-resistance condensation model as sub-functions.

The adaptive time step was adopted. The maximum and minimum time steps were 5×10^{-5} and 1×10^{-6} . In order to ensure the accuracy of numerical simulation, the Kuran number [13] was controlled within 0.5 during the calculation.

2.4. Results of Calculation and Analysis

(1) Distribution of the saturated steam in the downcomer

The distribution of saturated steam in the space is shown in Figure 4.

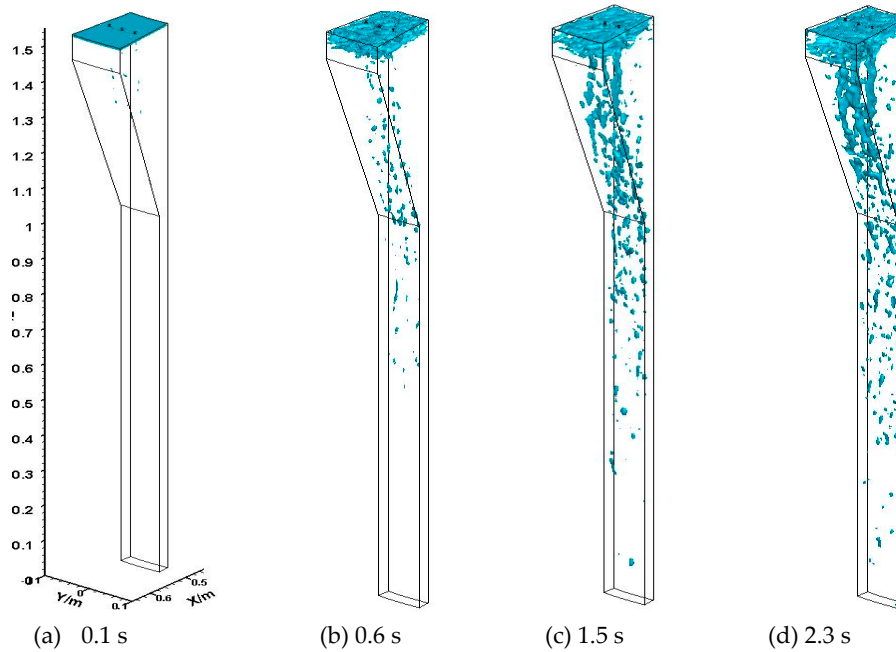


Figure 4. Volume of the top section with the vapor fraction at different times.

As shown in Figure 4, when the saturated steam and subcooled water continuously flowed into the steam generator, part of the saturated steam which had not been condensed was accumulated gradually, and forced into the lower downcomer by the rapidly injected subcooled water. It can be seen from Figure 4 that the steam has entered the lower downcomer at 0.6 s and arrives close to the exit at 1.3 s.

By assuming the height of the feed water ring is 0 mm, the height above the feed water ring is negative while it is positive below the feed water ring. The different height sections were chosen to display the vapor volume fraction after 2.8 s (Figure 5). Figure 5 is consistent with Figure 6d. The steam accumulation occurred in the upper part of the steam generator and the vapor volume fraction at the exit of downcomer is close to 0.

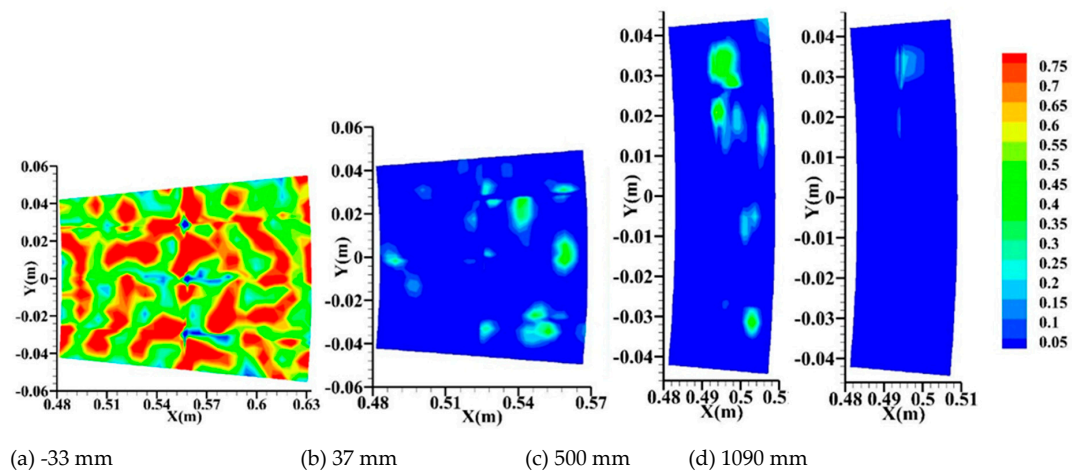


Figure 5. Vapor volume fraction at different sections after 2.8 s.

(2) Distribution of velocity field in the downcomer

Figure 6 describes the velocity diagram incorporating the nephograms of the vapor volume fraction in the detection plane $y = 0$.

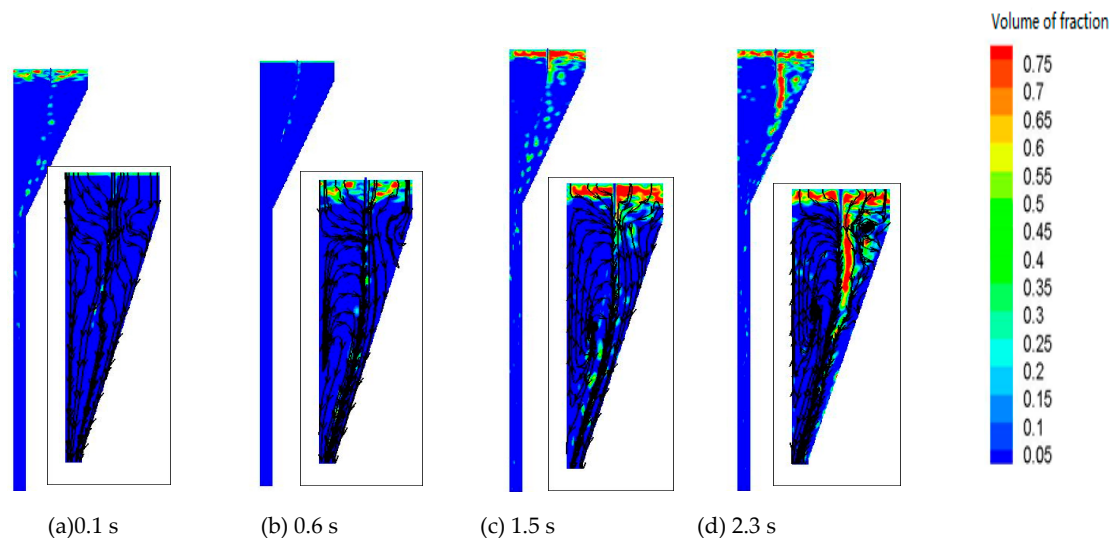


Figure 6. Velocity diagram incorporating the nephograms of the vapor volume fraction at different times.

Under certain inlet parameters of the saturated steam and subcooled water, the direct-contact condensation process of the high-speed subcooled water and saturated steam in the steam generator shows a stable flow pattern. Furthermore, there is an obvious vapor-liquid interface between the steam zone and the liquid zone. In the subcooled water zone, the subcooled water has a higher velocity than the steam, momentum, and energy at the inlet, keeping the single-phase transparent state. In the upper part of the subcooled water area, the saturated steam is affected by the low-pressure area at the inlet of the subcooled water, therefore, the speed increases. At the same time, due to the decrease of pressure, the saturated steam contained in the saturated water constantly precipitates out, producing a small number of bubbles.

As shown in Figure 6, a strong momentum and energy exchange between the subcooled water and the saturated steam exists in the phase boundary. This makes the saturated steam velocity near the phase boundary higher, thus producing a reflux vortex in the bottom left and upper right of the phase interface. Under the action of the reflux vortex, a drastic mixing occurs in the steam generator faster stabilizing the flow state.

(3) Distribution of temperature in the downcomer.

The distribution of temperature in the downcomer is reported in Figure 7. For the analysis, the saturated water was set as the initial field. As the inlet velocity of subcooled water was large, the temperature fluctuation phenomenon, induced by turbulent penetration in the steam generator, occurred and ranged from 430 K to 495 K. Indeed, there was an evident temperature transition zone near the vapor-liquid interface, which suggests that the heat transfer between the vapor and liquid phase near the phase interface has taken place.

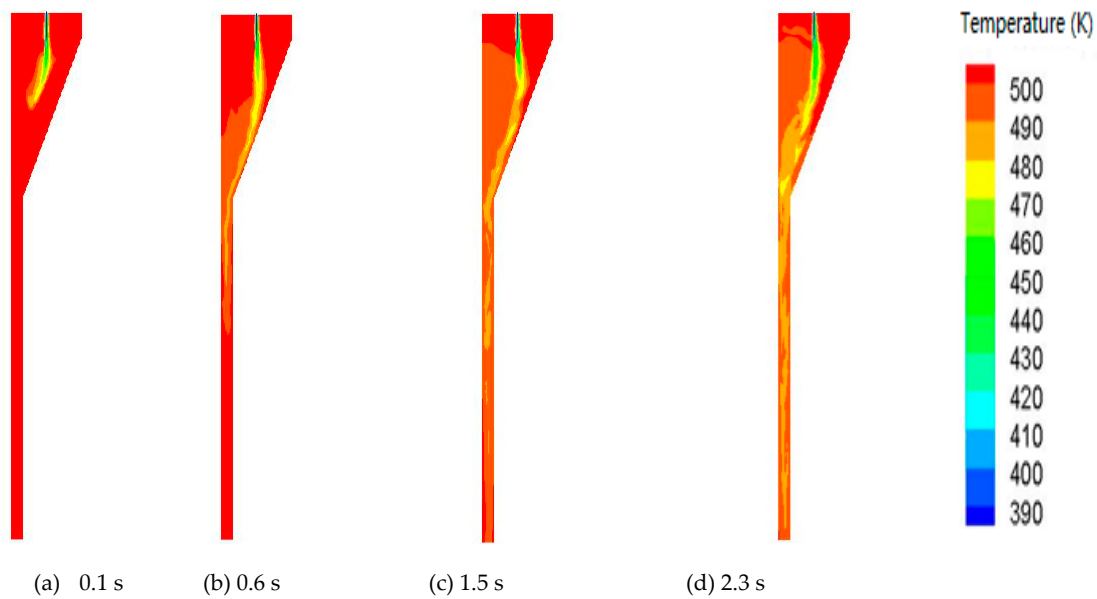


Figure 7. Temperature distribution in the downcomer.

Figure 7 illustrates the turbulent penetration phenomenon in the lower area of the subcooled water inlet and the temperature mixing phenomenon in the whole area of the downcomer after 1.5 s. The vortices near the inlet have been generated by the high inlet velocity of the subcooled water, accelerating the mixing process of vapor-liquid phases and, thus, resulting in chaotic temperature fluctuations. After 2.0 s, the temperature in the steam generator is relatively stable and fluctuated at approximately 484 k. There is a distinct temperature mixing zone near the inlet of the downcomer, where high and low temperature alternate occurred.

The section at 1090 mm from the feed ring was selected to show the temperature distribution at different times in Figure 8.

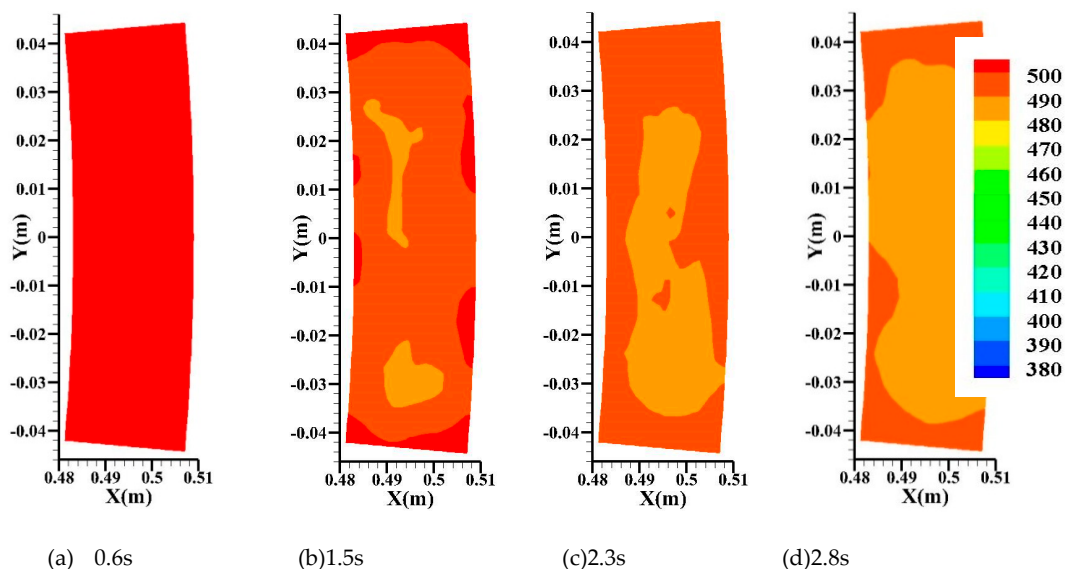


Figure 8. Temperature distribution at section 1090 mm from the feed water ring.

With the increase of subcooled water flow into the downcomer, its influence range gradually increases, and the average temperature of the same section in the downcomer decreases with the increase of time. Figure 8 illustrates the temperature mixing phenomenon in the section at 1090 mm of the downcomer after 1.5 s. The average temperature of the section is approximately 488 K after 2.8 s.

The different height sections were chosen to display the distribution of temperature after 2.8 s (Figure 9). The section at 500 mm from the feed water ring is a shrink. Being affected by the backflow and shrinkage structure, the influence area of the subcooled water is large. The flow velocity increases at shrinkage and carries the steam down to the narrow channel, making the steam condensing in the channel.

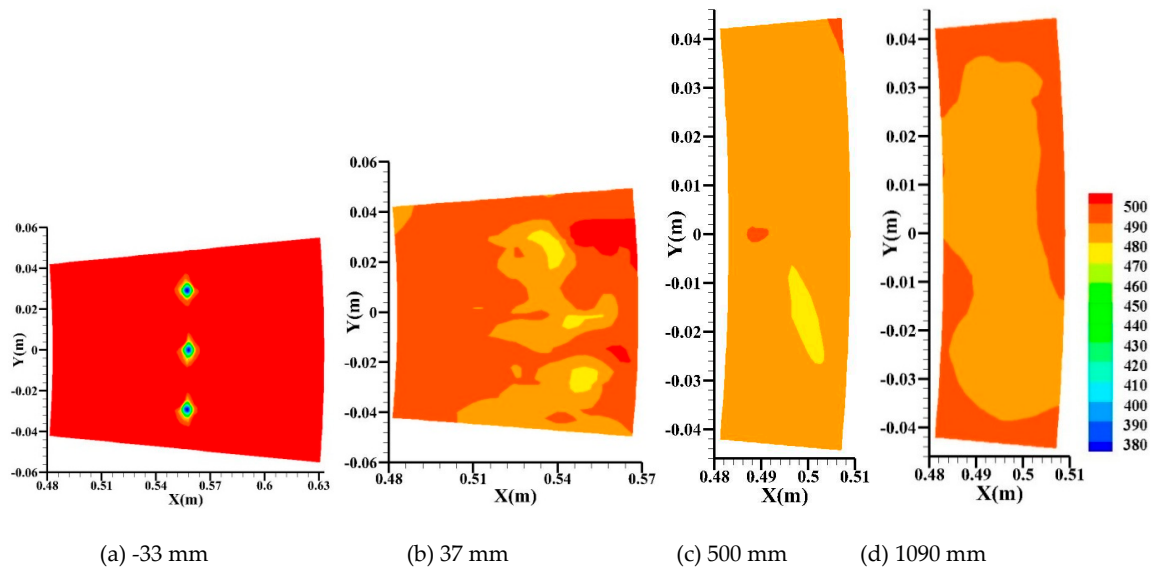


Figure 9. Temperature distribution at different sections after 2.8 s.

The negative pressure generated by condensation makes the hot fluid to fill in from the wall to the center. As a consequence, the influence range of cold fluid decreases while the temperature in the channel increases slightly. By assuming the height of feed water ring is 0 mm, the height above the feed water ring is negative while it is positive below the feed water ring.

3. Experimental Section

To simulate the operating environment of the natural circulation steam generator, a small steam generator simulator and an experiment loop were designed in accordance with a typical power plant system.

3.1. Experimental Loop

The experiment loop diagram is shown in Figure 10. The high-temperature and high-pressure water loop is a closed circle, while the high-temperature and high-pressure waters flow through the heat transfer tube in experimental apparatus under the driving of the shield pump, which is used to simulate the heat transfer from the reactor coolant loop to the steam-generator feed water. The steam generator feed water enters the experimental apparatus under the driving of the feed-water centrifugal pump and produces saturated steam flowing through the steam separator after absorbing the heat. The main saturated steam enters the condenser along the steam pipeline and then reenters the heat-exchange space forced by the feed-water pump. Henceforth, one circulation ends, and the next cycle begins.

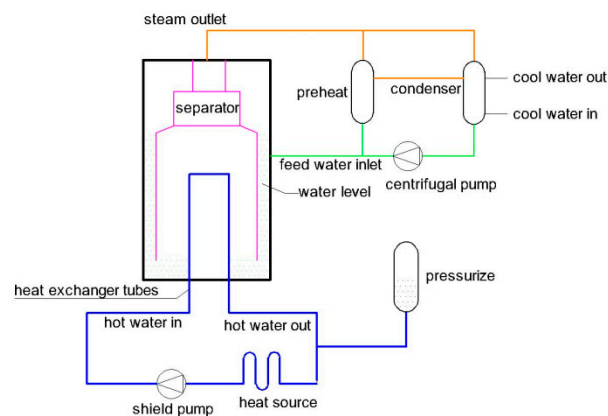


Figure 10. Schematic diagram of the experiment loop.

The high-temperature and high-pressure water loop are designed with a cold pressurizer to stabilize the loop pressure. The loop working pressure can reach a maximum of 17.5 MPa, whereas the maximum temperature is 320 °C.

The feed-water loop is designed with a preheater that can adjust the feed-water temperature in conjunction with the condenser. The adjustment range is 40–120 °C, while the steam production can reach up to 40 t/h.

3.2. Experimental Body Design

To simulate the operation of the steam generator, the principle of geometric similarity was adopted in the experimental body design. The double cylinders of carbon steel, forming the annular space, were used to simulate the steam generator downcomer. As shown in Figure 11, the double cylinders are divided into an outer and an inner sleeve. The inner sleeve is suspended below the steam separator, forming an annular space with the outer sleeve wall. The lower part of the inner sleeve and the bottom section of the outer sleeve form a baffling region so that water can smoothly enter the ascending channel and exchange heat with the high-temperature and high-pressure water loop.

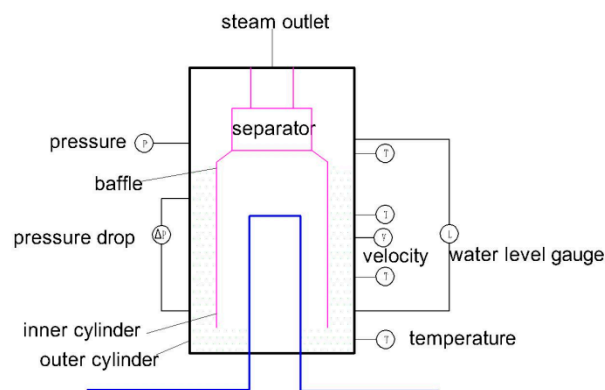


Figure 11. Diagram of the experimental body measurement point arrangement.

The feed water flows down the annulus due to the block of the baffle and inner sleeve. After entering the experimental body, it is deflected at the lower portion of the inner sleeve and then enters the ascending channel getting heated to saturated steam. To monitor the fluid state in the downcomer, the feed-water temperature sensor, the velocity sensor, and the pressure sensor were arranged along the flow direction of the feed water. The section at 500 mm below the feed water ring is taken as the reference of the 0 m plane, and the distance from the reference increases along the direction of the flow (from top to bottom). The positions of all measurement points are reported in Table 1.

Table 1. Positions of measurement points.

Name	Position (Flow Direction Is Positive)	Number
K type thermocouple	500/1090/1640/2190/2740/2940 mm	6
Pressure transmitter	1640 mm	1
Differential pressure transducer	−110/290/590/2590 mm	3
Local water level indicator	-	1
Velocity sensor	1640 mm	3

3.3. Measurement Accuracy

The data were collected by the fluke2645 collector at an acquisition rate of 1 Hz. The precision of measuring equipment is shown in Table 2.

Table 2. Precision of measuring equipment.

Name	Precision	Number
K type thermocouple	Class I industrial level	6
Pressure transmitter	0.2%	1
Differential pressure transducer	0.2%	3
Local water level indicator	-	1
Velocity sensor	1%	3
Distributor	0.1%	4
Collector	0.02%	1

3.4. Evaluation of Measurement Uncertainty

The uncertainty of measurement mainly comes from two aspects: First, under the same measurement conditions, the measured values change randomly, which is an inevitable random influence caused by the comprehensive factors in the measurement; second, the limitation of the instrument measurement performance and the uncertainty of the measurement instrument precision. This section evaluates the uncertainty of the pressure, temperature, and flow rate according to the class A and class B numerical evaluation methods of the uncertainty of measurement results [24].

(1) Uncertainty evaluation class A

Class A evaluation is obtained from a series of measurement data. The arithmetic mean value is adopted as the measurement result in the test. The uncertainty of class A evaluation is [24]:

$$u_A = s(\bar{x}) = \frac{s(x)}{\sqrt{n}} = \sqrt{\frac{\sum_{i=1}^n (x_i - \bar{x})^2}{(n-1)n}} \quad (24)$$

where n is the number of measured data.

(2) Uncertainty evaluation class B

Class B evaluation is based on the probability distribution of the data or calibration certificates. This section employs uniform distributions to calculate the standard uncertainty caused by the intrinsic error of the instrument. The calculation formula is [24]:

$$u(x) = \frac{x_m \times s\%}{\sqrt{3}} \quad (25)$$

where x_m is the instrument range; s is the instrument precision; and $x_m \times s\%$ represents the maximum error limit that an instrument may achieve.

(3) Synthesis standard uncertainty

The synthesis standard uncertainty derives from multiple components as follows [24].

$$u_s = \sqrt{u_A^2 + u_m^2 + u_b^2 + u_c^2} \quad (26)$$

where u_A represents uncertainty evaluation class A; u_m corresponds to the uncertainty caused by instrument measurement error; u_b represents uncertainty caused by distributor; and u_c is the uncertainty caused by collector.

With a 95% confidence interval, the uncertainty of pressure difference measurement is 1%, while the uncertainties of temperature and velocity measurements are 0.2% and 15%, respectively.

4. Results and Discussion

4.1. Effect of the Saturated Steam Carried Downward on the Temperature in the Downcomer

The typical temperature distribution in a downcomer is displayed in Figure 12. The ordinate value is the ratio of the temperature and the saturation temperature at its corresponding pressure, while the abscissa value indicates the installation height of the temperature measurement point (i.e., 500 mm below the feed water ring is taken as the benchmark of the 0 m plane). The experimental data show that the temperature in the downcomer gradually decreases from the inlet to the lowest point at 1640 mm below the feed water ring and then rises slightly. This indicates that the steam carried downward is in direct contact with the channel and hereby condenses, while the water absorbs the latent heat of the steam, leading to a slight rise in temperature. In the experiment process, the temperature difference between the section at 500 mm below the feed water ring and the section at 3000 mm below feed water ring is less than 1.5 °C. The trend of the calculated data is consistent with that of the experimental data, but the lowest temperature is 500 mm below the feed water ring. The discrepancy between the calculated and the experimental values may arise from the difference in the calculation accuracy and the difference between the actual measurement point and the temperature value extraction point.

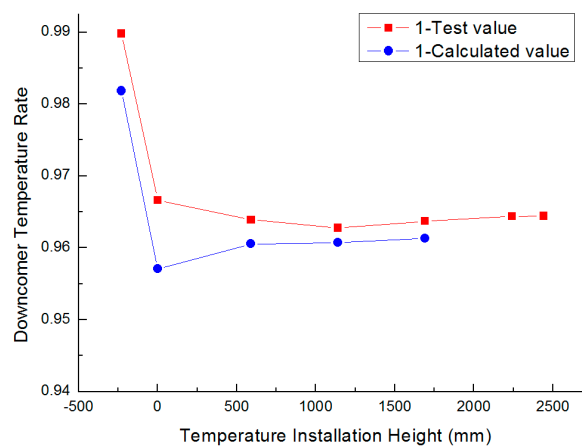


Figure 12. Calculated and tested temperature at different sections.

4.2. Effect of Saturated Steam carried Downward on the Pressure-Drop in the Downcomer

(1) Pressure-drop and subcooling degree in the downcomer

The pressure-drop of different height differences in the downcomer measured in the experiment is shown in Figure 13. Notably, 500 mm below the feed water ring is taken as the benchmark of 0 m plane. Three different heights of −110 mm, 290 mm, and 590 mm, between which the height of 2590 mm and the pressure-drop has been analyzed, were selected along the flow direction. They are 2.7 m, 2.3 m, and 2 m in the figure, respectively. The abscissa value is the subcooling degree of the mean temperature of the medium in the downcomer. It can be seen from the figure that the general trend of the pressure-drop of different height difference in the downcomer is in line with that of the variation

in the subcooling degree. Furthermore, as the condensation of saturated steam carried downward is affected by multiple factors, such as the subcooling degree and fluid velocity, the pressure-drop has a nonlinear relation with the subcooling degree. The reason for the abrupt decline in the pressure-drop in the downcomer is that the fluid velocity is lower (1.76 m/s) when the subcooling degree is 20.4 °C, and the amount of recirculation water is small so that the amount of saturated steam carried downward decreases under this experimental condition. When the subcooling degree is 22.5 °C, the fluid velocity is higher (1.87 m/s), and the amount of recirculation water is larger at this experimental condition so that the amount of saturated steam carried downward increases and the pressure-drop in the downcomer decreases.

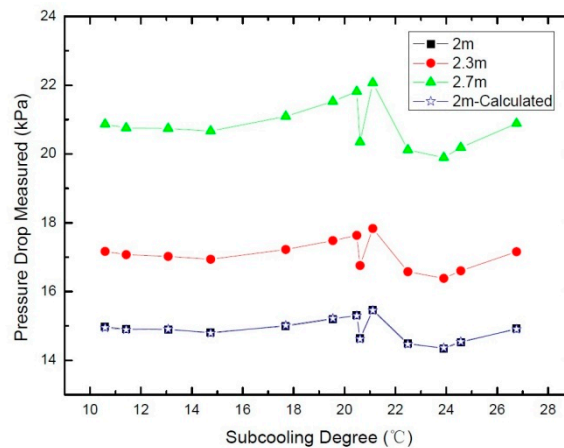


Figure 13. Pressure-drop and subcooling degree in the downcomer.

(2) Pressure-drop and velocity in the downcomer

The pressure-drop of the variant height difference in the downcomer has the same trend with velocity distribution. The velocity, as one of the factors affecting the steam condensation in the downcomer, also shows a nonlinear correlation with the pressure-drop variation, as can be seen in Figure 14. In the figure, the abscissa value is the mean velocity value of the medium measured at the height of 1640 mm with different angles (35°/125°/215°). With the increase of velocity, the pressure-drop of the varying height difference changes within 2.5 kPa. Moreover, as the height away from the tube sheet increases, the influence range of the saturated steam carried downward increases, raising the variation in pressure-drop accordingly. Between the velocity range from 1.6 to 2.0 m/s, the inlet steam quality and the temperature in downcomer are non-linear, and the pressure-drop is fluctuating.

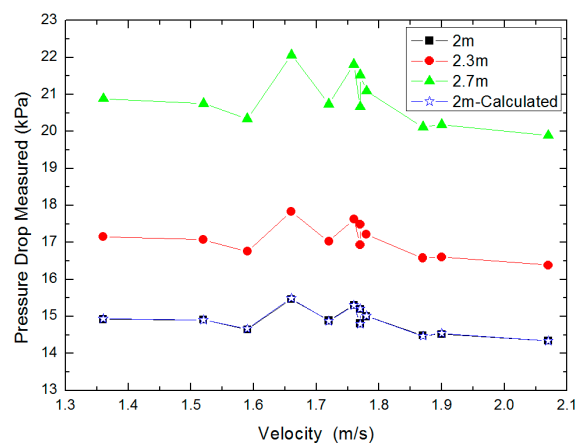


Figure 14. Pressure-drop of varying height difference and velocity in the downcomer.

As shown in Figure 15, when the velocity is less than 1.68 m/s, the subcooling degree increases with the increase of velocity at the experimental condition. As a consequence, the condensation rate increases quickly. The increasing rate of the friction pressure-drop in the downcomer is higher than the accelerating pressure-drop, while the gravity pressure-drop is unchanged. Therefore, the total pressure-drop decreases slightly. Indeed, the acceleration pressure-drop is mainly related to the variation of the void fraction in the inlet cross-section. The frictional pressure-drop mainly relies on the product of the full liquid phase conversion coefficient and liquid phase frictional resistance, whereas the full liquid phase conversion coefficient is also related to the change of the void fraction. Therefore, the acceleration pressure-drop changes as a function of the frictional pressure-drop.

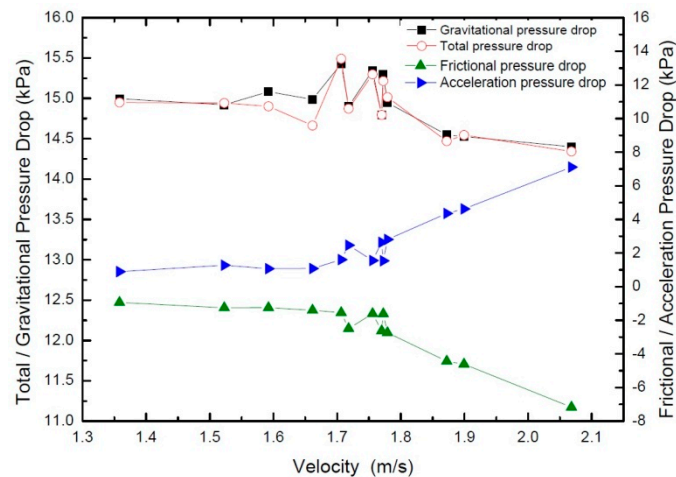


Figure 15. Trend of pressure-drop with velocity in the downcomer.

The acceleration pressure-drop increases with the friction pressure-drop when the velocity is higher than 1.68 m/s. However, in the case of a velocity within the 1.68–1.74 m/s range, the mean temperature increases by 20 °C in the experimental condition; the density and the gravity pressure-drop decrease; the total pressure-drop decreases. In contrast, in the case of higher velocity values, the trend of the total pressure-drop depends on the gravity pressure-drop value. With the change of the temperature and void fraction, the gravity pressure-drop and the total pressure-drop decrease.

(3) Resistance coefficient and Reynolds number in the measurement domain

The flow cross-section in the measurement domain of the downcomer remains constant. The pressure-drop mainly consists of gravitational, frictional, and acceleration pressure drops. Then, the resistance coefficient in the downcomer can be calculated according to the flow resistance formula [25]:

$$\xi = \frac{2\Delta P}{\rho v^2} \quad (27)$$

The correlation between the resistance coefficient and Reynolds number is shown in Figure 16.

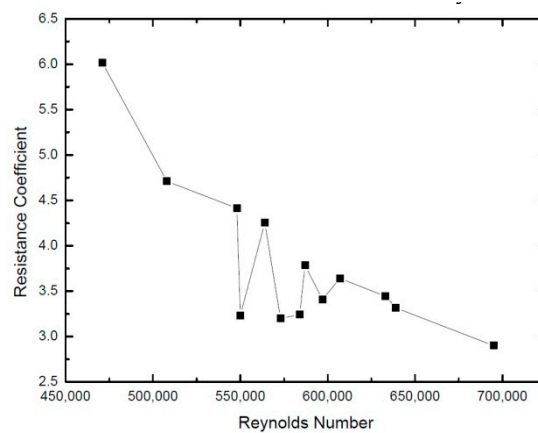


Figure 16. Resistance coefficient and Reynolds number in the downcomer.

As shown in Figure 16, the value of the resistance coefficient in the downcomer reduces as the Reynolds number increases. On the one hand, the saturated steam carried by the saturated water to the downcomer affects the density in the channel, thereby changing the gravitational pressure-drop. On the other hand, as steam condenses, the acceleration pressure-drop and frictional pressure-drop also change accordingly. However, the resistance characteristics differ from those of single-phase fluid. Therefore, the pressure-drop variation can be considered as a monitoring indicator of the saturated steam carried downward entering the downcomer. When it undergoes a nonlinear change between the pressure-drop parameter and the Reynolds number, the existence of two-phase flow can be considered.

4.3. Effect of Saturated Steam Carried Downward on Density in the Downcomer

The density is calculated according to the measured pressure and temperature values in the downcomer (reported as Calculated by Temperature and Calculated by Pressure Drop in Figure 17). In Figure 17, the left ordinate value is the ratio of the calculated density to the density of saturated water, while the right side is the logarithm of temperature in the downcomer ($t_x = \ln(t/100)$ where t is the temperature in the downcomer). In the downcomer, after the feed water mixes with the recirculation water, the whole temperature is lower than the saturation temperature, therefore, the density calculated by the temperature is higher than saturated water. When the velocity is less than 1.7 m/s, the calculated density obtained by temperature fluctuates approximately within 3% when the mean temperature in the downcomer changes. The calculated density obtained by the pressure-drop is lower than saturated water. Furthermore, the densities calculated by these two methods differ from each other by a factor ranging from 4% to 10%.

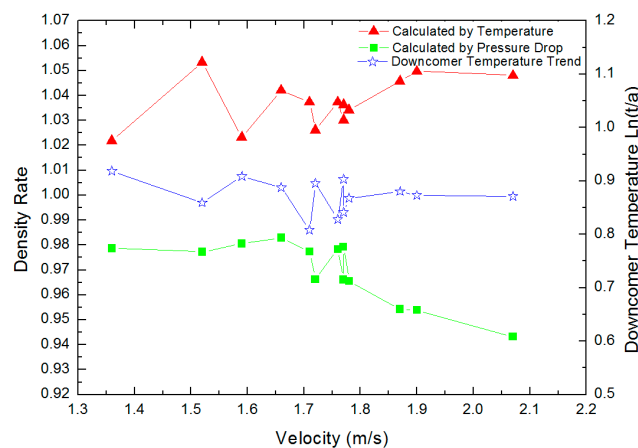


Figure 17. Density ratio and velocity in the downcomer.

Figure 18 illustrates the ratio of the water level calculated by the corrected density and the local water level. The deviation of the water level calculated by the pressure-drop correction and density modification using the mean temperature in the downcomer can reach a maximum of 5%, with the mean goodness of the fit between the local water level value and that calculated by pressure-drop correction being 99.7%. This indicates that the density calculated by the pressure-drop correction is more representative.

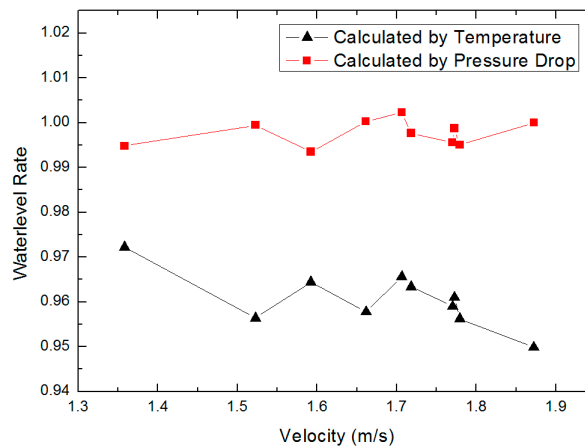


Figure 18. Water level ratio and velocity in the steam generator.

The actual density in the downcomer is lower than that calculated by the temperature correction. The main reason for this discrepancy is the presence of saturated steam carried downward.

4.4. Steam Quality Trend in the Downcomer

The total mass rate of saturated steam is the vapor content in the downcomer. The initial vapor rate at the inlet was set, while the measured parameters such as the temperature, pressure, and velocity were set as input values. The convergence condition set as the pressure-drop deviation between the calculation value and the test value should be less than 0.5%. The average mass vapor content rate of the downcomer was calculated iteratively. It was assumed that i) the medium in the downcomer had no heat exchange with the metal sleeve on both sides, ii) the inlet boundary condition was velocity, and iii) the outlet boundary condition was pressure.

According to the internal structures of the steam generator, the section under 500 mm below the feed water ring in the steam generator downcomer was analyzed using a homogeneous flow model and divided into some small domains with equal height from the top to bottom. Each region is denoted by small index i .

The conservation of mass in each region implies that the sum of liquid mass m_{li} and vapor phase mass m_{si} in each region is equal.

$$m_i = m_{li} + m_{si} = m_{i-1} \quad (28)$$

The outlet pressure P_{io} in each area is equal to the sum of the inlet pressure P_{ii} , the frictional pressure-drop ΔP_{if} , the accelerated pressure-drop ΔP_{ia} , and the gravitational pressure-drop ΔP_{ig} as follows.

$$P_{io} = P_{ii} - \Delta P_{if} - \Delta P_{ia} + \Delta P_{ig} \quad (29)$$

Here, the two-phase frictional pressure-drop ΔP_{if} equals the whole liquid phase conversion coefficient φ_{il} multiplied by the liquid phase frictional pressure-drop [26].

$$\Delta P_{if} = \varphi_{il}(\Delta P_{if})_l \quad (30)$$

The conversion coefficient of the total liquid phase was calculated by average viscosity [26]:

$$\varphi_{il} = [1 + x_i(\frac{v_{is}}{v_{il}} - 1)][1 + x_i(\frac{\mu_{il}}{\mu_{is}} - 1)]^{-0.25} \quad (31)$$

where x_i is the rate of mass vapor content; v_{is} is the vapor phase velocity; and v_{il} is the liquid phase velocity. Assuming that the vapor phase velocity is consistent with the liquid phase velocity, the whole liquid phase conversion coefficient is:

$$\varphi_{il} = [1 + x_i(\frac{\mu_{il}}{\mu_{is}} - 1)]^{-0.25} \quad (32)$$

The liquid phase friction resistance is [26]:

$$(\Delta P_{if})_l = \frac{\lambda_l l_i \rho_{im}}{2d_i} v_i^2 \quad (33)$$

where λ_l is the liquid phase frictional coefficient; l_i is the flow channel length; ρ_{im} is the average density; d_i is the equivalent diameter; and v_i is the velocity. The two-phase gravitational pressure-drop can be expressed as [26]:

$$\Delta P_{ig} = \rho_{im} g l_i \quad (34)$$

The two-phase accelerated pressure-drop can be expressed [26] as:

$$\Delta P_{ia} = G^2 \left\{ \left[\frac{(1 - x_i)^2}{\rho_{il}(1 - \beta_i)} + \frac{x_i^2}{\rho_{is}\beta_i} \right] - \left[\frac{(1 - x_{i-1})^2}{\rho_{i-1l}(1 - \beta_{i-1})} + \frac{x_{i-1}^2}{\rho_{i-1s}\beta_{i-1}} \right] \right\} \quad (35)$$

where G is the mass flow per unit area; ρ_{il} is the density of the liquid phase; ρ_{is} is the density of the vapor phase; and β_i is the vapor rate of the volume. In the calculation domain, the condensation calculation refers to Equations (13)–(23).

The computational process is shown in Figure 19.

The correlation between the mean steam quality in the downcomer and subcooling degree and the velocity is displayed in Figure 20.

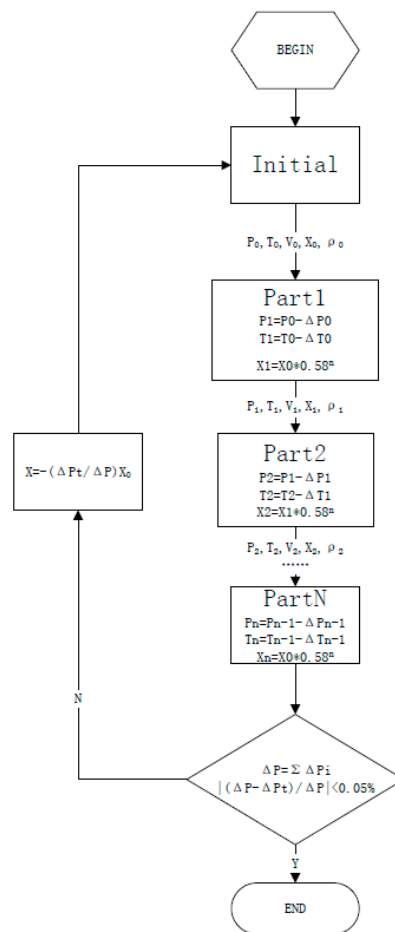


Figure 19. Computation flowchart.

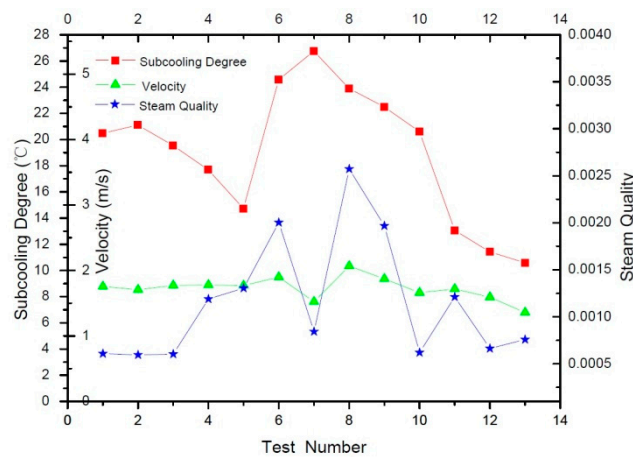


Figure 20. Mean steam quality trend in the downcomer.

As shown in Figure 20, for all the experimental conditions, the mean steam quality is lower than 0.27%. The operating parameters of experiment 2 are close to the physical parameters of the calculated case in Figure 5, the relative deviation between steam quality obtained by test pressure-drop (0.06%) and steam quality obtained by CFD calculation (0.074%) is 19%, which is mainly caused by the deviation of the velocity and subcooled water temperature. When the velocity is lower than 1.8 m/s, with the reduction of subcooling degree, the condensation amount of saturated steam carried downward decreases, and the steam quality increases slightly. When the velocity is higher than 1.8 m/s,

even though the subcooling degree increases, the recirculation water amount in the steam generator increases so that the amount of saturated steam carried downward increases. In the meantime, the increase of velocity can lead to an insufficient mixing between the recirculation saturated water and feed water at the inlet of the downcomer, which is bad for the condensation of the saturated steam carried downward, resulting in an increase in steam quality in the downcomer. When the velocity decreases but the subcooling degree increases, the condensation of saturated steam in the downcomer accelerates, leading to a drop in the steam quality in the downcomer, as it can be observed in experiment 7.

After the velocity in the downcomer has increased to a certain value, the sensitivity of steam quality in the downcomer to the subcooling degree begins to decline. Therefore, it is recommended that the fluid velocity in the downcomer should be adequately controlled in the design of the steam generator. Moreover, the subcooling degree in the downcomer is supposed to be controlled above 20 °C, and, at the same time, in case too much saturated steam is carried downward to the downcomer, the structure of the separator needs to be improved.

5. Conclusions

The saturated steam influences the density and resistance in the downcomer and might affect the stability of the water cycle in the secondary loop. To investigate the condensation state of the saturated steam carried to the narrow downcomer in the direction of the top to bottom and its influence on the flow characteristics in the downcomer, a mathematical model of the downcomer was established based on the internal structures of a natural circulation steam generator. The simulator was designed, and the experiment loop was built according to the internal structures of the steam generator. However, the effect of saturated steam carried downward on the properties in the downcomer was studied.

- (1) Affected by the saturated steam carried downward, the fluid temperature in the downcomer first decreases due to the mixing of hot and cold fluids and then slightly rises due to the absorption of heat released by the steam contact condensation. The temperature difference between the section at 500 mm below the feed water ring and the section at 3000 mm below feed water ring is less than 1.5 °C.
- (2) The pressure-drop measurement in the downcomer can be taken as a monitoring parameter to justify whether the saturated steam carried downward enters the downcomer or not. When pressure-drop is nonlinear with the Reynolds number, the presence of two-phase flow shall be considered.
- (3) The deviation of the water level calculated by the pressure-drop correction and density modification using the mean temperature in the downcomer can reach a maximum of 5%, with the mean goodness of the fit between the local water level value and that calculated by pressure-drop correction being 99.7%. The density corrected by the pressure-drop, which was measured at the domain under 500 mm below the feed water ring, is more reliable than that corrected by temperature for water level computation.
- (4) When the velocity in the downcomer is constant, with the reduction of the subcooling degree, the condensation amount of saturated steam carried downward decreases, while the void fraction in downcomer increases.
- (5) When the velocity is increasing to 1.8 m/s, the sensitivity of the steam quality in the downcomer to the subcooling degree begins to diminish as the velocity continues to rise.
- (6) The one-dimensional calculation program based on the measured pressure difference here developed can be employed to analyze the pressure, temperature, and void fraction distributions in the downcomer. The computation results are in excellent agreement with the experimental results, which helps simplify the internal calculation of the steam generator and improve calculation efficiency.

In future work, the effect of the steam generator separator structure on the steam carried downward will be researched to fundamentally reduce the steam carried downward and improve the stability of the secondary side operation.

Author Contributions: Conceptualization, X.W. and Y.L.; methodology, Y.L.; software, Y.L.; validation, H.S., C.G. and R.T.; formal analysis, Y.L.; investigation, Y.L.; resources, C.G.; data curation, Y.L.; writing—original draft preparation, Y.L.; writing—review and editing, R.T.; visualization, Y.L.; supervision, X.W.; project administration, H.S.; funding acquisition, X.W.

Funding: This research was sponsored by the National Natural Science Fund (NO.51676052).

Acknowledgments: The authors want to thank Chen Yinqiang, Tang Yi, Lu Yuanshu, Mao Feng, Zhan Chunyuan, and Yu Shengzhi. The authors would also like to express appreciation to Lu Tao (Beijing University of Chemical Technology) for his support for the research work. Furthermore, the authors thank Xiong Changhuai for the fruitful discussion on the subject.

Conflicts of Interest: The authors declare no conflict of interest. The funders had no role in the design of the study; in the collection, analyses, or interpretation of data; in the writing of the manuscript, or in the decision to publish the results.

Nomenclature

The subscript i indicates section i of the computation domain; the subscript l indicates the liquid phase; and the subscript s indicates the vapor phase.

P	Steam pressure, Pa;
ρ_m	Medium density in the downcomer, kg/m^3 ;
H	Height of downcomer, m;
ρ_x	Density of the preheating section in ascending channel, kg/m^3 ;
H_x	Height of the preheating section in ascending channel, m;
ρ_{xs}	Density of the vapor in the ascending channel, kg/m^3 ;
H_{xs}	Height of the void space in ascending channel, m;
ΔP_r	Pressure drop in the rising section, Pa;
ΔP_{sp}	Pressure drop in the steam separator, Pa;
m	Mass, kg/s;
P_{io}	Outlet pressure, Pa;
P_{ii}	Inlet pressure, Pa;
ΔP_{if}	Frictional pressure drop, Pa;
ΔP_{ia}	Acceleration pressure drop, Pa;
ΔP_{ig}	Gravitational pressure drop, Pa;
φ_{il}	Full liquid-phase conversion coefficient
x_i	Steam quality
μ	Dynamic viscosity, $\text{N}\cdot\text{s/m}^2$;
λ_i	Friction coefficient;
l_i	Length of flow channel, m;
ρ_{im}	Density of water-vapor mixture, kg/m^3 ;
d_i	Equivalent diameter, m;
v	Velocity, m/s;
G	Mass flow rate per unit area, $\text{kg}/(\text{m}^2 \text{ s})$;
β_i	Volume void fraction;
d_1	Reference mean diameter bubble, $1.5 \times 10^{-3} \text{ m}$;
d_0	Reference mean diameter bubble, $1.5 \times 10^{-4} \text{ m}$;
θ	Subcooling degree of liquid phase, $^\circ\text{C}$;
θ_1	Reference subcooling degree of the liquid phase, $0 \text{ }^\circ\text{C}$;
θ_0	Reference subcooling degree of the liquid phase, $15 \text{ }^\circ\text{C}$;
k_{if}	Thermal conductivity of the liquid phase, $\text{w}/(\text{m k})$;
Re	Reynolds number;
Pr	Prandtl number;
H_{il}	Enthalpy of saturated water, kJ/kg ;
H_{is}	Enthalpy of saturated steam, kJ/kg .

References

1. Sun, Z.N. The working principle and structure design of steam generator. In *Nuclear Power Facility*; Harbin Engineering University Press: Harbin, China, 2004; Chapter 2, pp. 11–21.
2. Steam Generator Writing Group. Hydrodynamics of steam generator. In *Steam Generator*; Atomic Energy Press: Beijing, China, 1982; Chapter 3, pp. 159–161.
3. Woods, B.G.; Groome, J.; Collins, B. An assessment of PWR steam generator condensation at the Oregon State University APEX facility. *Nucl. Eng. Des.* **2009**, *239*, 96–105. [[CrossRef](#)]
4. Woods, B.G.; Collins, B. RELAP5-3D modeling of PWR steam generator condensation experiments at the Oregon State University APEX facility. *Nucl. Eng. Des.* **2009**, *239*, 1925–1932. [[CrossRef](#)]
5. Brucker, G.G.; Sparrow, E.M. Direct contact condensation of steam bubbles in water at high pressure. *Int. J. Heat Mass Transf.* **1977**, *20*, 371–381. [[CrossRef](#)]
6. Yang, Y.L.; Sun, B.Z.; Yang, L.B.; Zhang, Y. Numerical simulation on vapor-liquid two-phase flow of the secondary circuit in steam generator. *At. Energy Sci. Technol.* **2012**, *46*, 51–56. (In Chinese)
7. Versteeg, H.K.; Malalasekera, M. Turbulence and its modeling. In *An Introduction to Computational Fluid Dynamics: The Finite Volume Method*; Prentice Hall Press: Upper Saddle River, NJ, USA, 2007; Chapter 3, pp. 40–113.
8. Shmatov, D.P.; Kruzhaev, K.V.; Afanasev, A.A.; Polval'nyi, E.S.; Kretinin, A.; Safonov, S.V. Simulation of Gas Flow in an Anti-Surge Valve by the ANSYS CFX Software Complex. *Chem. Pet. Eng.* **2018**, *53*, 662–667. [[CrossRef](#)]
9. Sun, D.L.; Xu, J.L.; Wang, L. A vapor-liquid phase change model for two phase boiling and condensation. *J. Xi'an Jiaotong Univ.* **2012**, *46*, 7–11. (In Chinese)
10. Yu, Y.Q.; Elia, M.; Aleksandr, O.; Justin, T. Aporous medium model for predicting the duct wall temperature of sodium fast reactor fuel assembly. *Nucl. Eng. Des.* **2015**, *295*, 48–58. [[CrossRef](#)]
11. Jiang, X.; Zhang, M.; Xie, Y.C.; Yao, W.D. Three-dimensional numerical simulation of secondary side flow field in steam generator. *At. Energy Sci. Technol.* **2008**, *42*, 438–443. (In Chinese)
12. Li, X.B.; Zhang, M.C.; Fang, X.L.; Zhang, Y.H. The flow field characteristics in the annular downcomer of SG secondary side. *J. North Chin. Electr. Power Univ.* **2013**, *40*, 86–90. (In Chinese)
13. Wang, F.J. Three dimensional turbulence model and its application in CFD. In *Computational Fluid Dynamics Analysis: Principles and Applications of CFD Software*; Tsinghua University Press: Beijing, China, 2004; Chapter 4, pp. 120–125.
14. Zhou, L.; Chong, D.T.; Liu, J.P.; Yan, J.J. Numerical study on flow pattern of sonic steam jet condensed into subcooled water. *Ann. Nucl. Energy* **2017**, *99*, 206–215. [[CrossRef](#)]
15. Shah, A.; Chughtai, I.R.; Inayat, M.H. Numerical simulation of direct-contact condensation from a supersonic steam jet in subcooled water. *Chin. J. Chem. Eng.* **2010**, *18*, 577–587. [[CrossRef](#)]
16. Gulawani, S.S.; Joshi, J.B.; Shah, M.S.; RamaPrasad, C.S.; Shukla, D.S. CFD analysis of flow pattern and heat transfer in direct contact steam condensation. *Chem. Eng. Sci.* **2006**, *61*, 5204–5220. [[CrossRef](#)]
17. Ranz, W.E.; Marshall, W.R., Jr. Evaporation from drops: Part I. *Chem. Eng. Prog.* **1952**, *48*, 141–146.
18. Li, S.Q.; Wang, P.; Lu, T. Numerical simulation of direct contact condensation of subsonic steam injected in a water pool using VOF method and LES turbulence model. *Prog. Nucl. Energy* **2015**, *78*, 201–215. [[CrossRef](#)]
19. Ji, B.; Chen, J. 3D structure mesh generation method. In *ANSYS ICEM CFD Detailed Examples of Grid Technology*; China Water Power Press: Beijing, China, 2012; Chapter 1, pp. 153–205.
20. Anglart, H.; Nylund, O. CFD application to prediction of void distribution in two phase bubbly flows in rod bundles. *Nucl. Eng. Des.* **1996**, *163*, 81–98. [[CrossRef](#)]
21. Hughmark, G.A. Mass and heat transfer from a rigid sphere. *AIChE J.* **1967**, *13*, 1219–1221. [[CrossRef](#)]
22. Koncar, B.; Mavko, B. Modeling of low-pressure subcooled flow boiling using the RELAP5 code. *Nucl. Eng. Des.* **2003**, *220*, 255–273. [[CrossRef](#)]
23. Yang, Z.; Huang, W.; Zhou, J. Study on steady state thermal hydraulic performance of steam generator with an axial economizer. *World Sci Tech R D* **2016**, *38*, 799–803.
24. Li, Y.Z.; Yuan, M.S. Dimensional analysis and similarity principle. In *Fluid Mechanics*; High Education Press: Beijing, China, 2008; Chapter 10, pp. 303–318.

25. The General Administration of Quality Supervision, Inspection and Quarantine of the People's Republic of China; The Standardization Administration of the People's Republic of China. *GB/T 27418-2017, Guide to Evaluation and Expression of Uncertainty in Measurement*; The General Administration of Quality Supervision, Inspection and Quarantine of the People's Republic of China; The Standardization Administration of the People's Republic of China: Beijing, China, 2017.
26. Yan, C. Two-phase flow pressure drop of straight pipe. In *Gas-Liquid Flow*; Harbin Engineering University Press: Harbin, China, 2001; Chapter 1, pp. 65–88.



© 2019 by the authors. Licensee MDPI, Basel, Switzerland. This article is an open access article distributed under the terms and conditions of the Creative Commons Attribution (CC BY) license (<http://creativecommons.org/licenses/by/4.0/>).